ARTICLE - SUPPLEMENT

1 Supplementary methods

1.1 Sample flow and sorting

In this section, we further illustrate the sorting principle with images of the operating device. First, Supplementary figure S1 shows an experiment where dye was added to the sample flow to visualize the flow at the sorting junction in the bright field. Three different moments are displayed: the initial flow (left), the flow shortly after a jet flow deflection (middle), and the deflected flow entering the sorting channel (right). The figure shows the narrow focusing of the sample flow in the centre of the main channel, which ensured a stable bead and cell position both for detection as well as deflection. The figure also shows how the sample flow continued fully into the waste channel unless it was deflected by the jet flow.

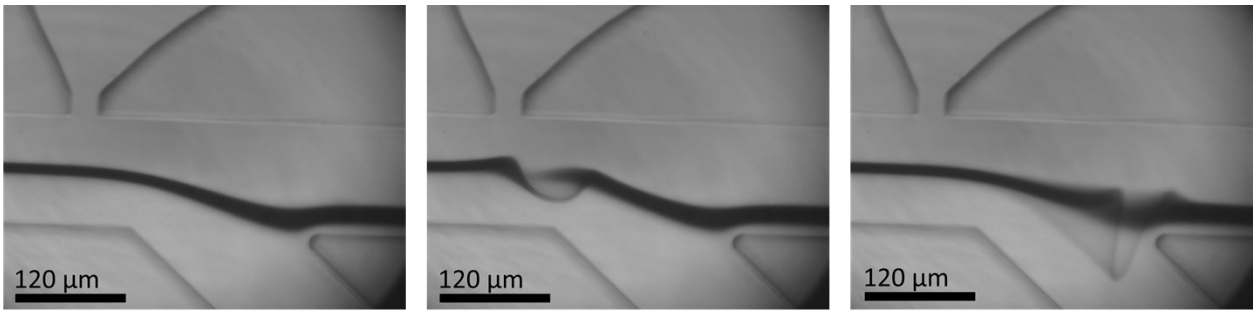

Supplementary figure S1: Dye flow experiment illustrating the narrow focusing of the sample flow in the main channel and the propagation of deflected dye into the sorting channel.

When sorting, we monitored the stability of the particle position at the detection spot and the stability of the deflection and sorting process through the live imaging in the fluorescent spectrum. Two example images are shown in Supplementary figure S2. The sorting was deactivated on the left image and all particles continued straight into the waste channel. The sorting was activated on the right image, leading to the deflection of the particles into the sorting channel.

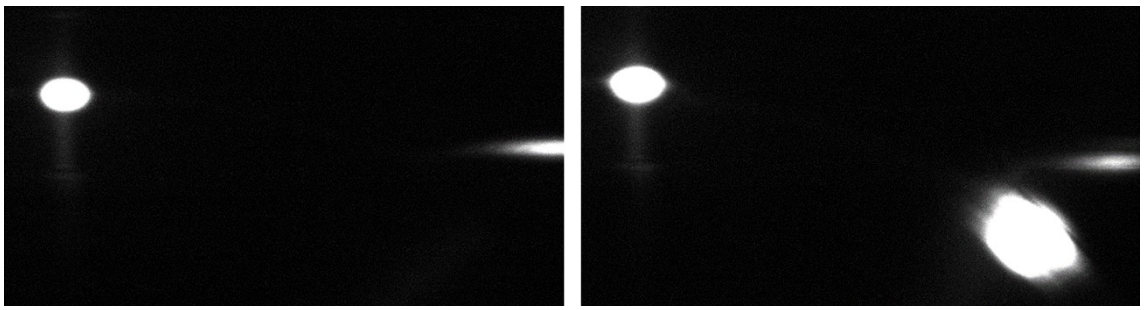

Supplementary figure S2: Images of fluorescent beads passing through the laser spots at the sorting junction. Initial flow with sorting deactivated (left) and during sorting with sorting activated (right).

1.2 Stack and fabrication

The bubble-jet cell sorter devices were fabricated onto 200 mm wafers using imec's 200 mm CMOS Pilot Line facilities. The chips consist of a stack of three bonded wafers: a bottom silicon wafer with the heaters, a middle silicon wafer containing the fluidic channels, and a quartz wafer for closing the fluidic channels and providing optical access. The main modules in the integration process flow are illustrated in Supplementary Figure S3 (a-h) while Supplementary Figure S4 shows a full 200-mm wafer of diced bubble-jet cell sorter chips.

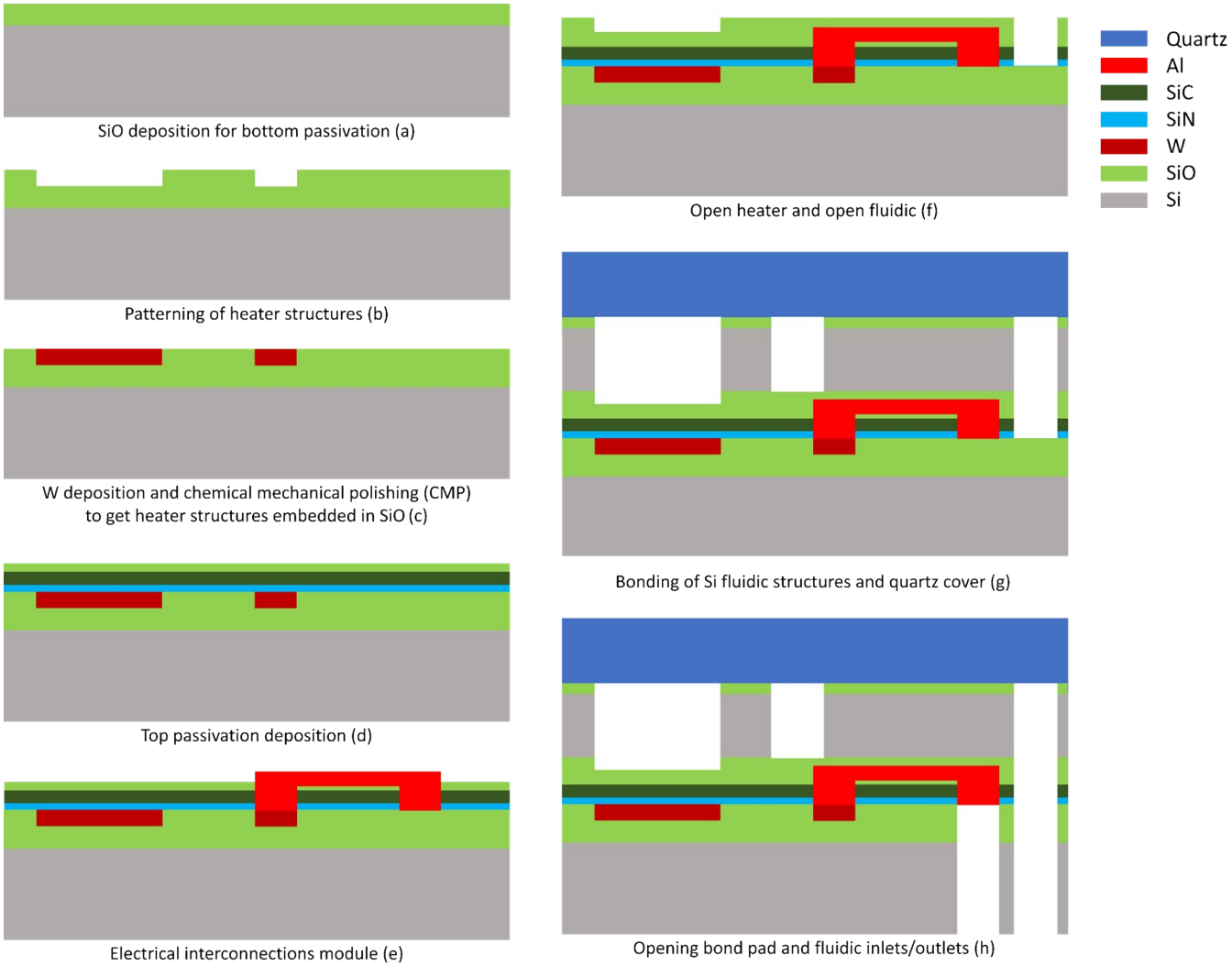

Supplementary Figure S3: Fabrication steps of the bubble-jet cell sorter devices as fabricated in the 200 mm CMOS Pilot Line facilities at imec. The schematics of the design and the layer thicknesses are not drawn to scale.

Heater wafer: First, 1 µm of wet thermal oxide was grown on a standard silicon (Si) wafer, which was followed by photolithography patterning and dry etching steps to form heater structures and electrical connection structures (a-b). Then, a thin liner stack was conformally deposited, after which the patterned heater structures were filled with Tungsten (W). A chemical mechanical polishing (CMP) process was applied to keep W only at the heater and electrical connection areas (c). On top of this layer, a passivation stack including silicon nitride (SiN), silicon carbide (SiC), and silicon oxide (SiO) was deposited (d). Afterwards, electrical via connection windows and bond pad areas were opened by photolithography patterning and etching. Aluminium (Al) was deposited, patterned, and dry etched to form the bond pad material and low resistance electrical interconnection traces (e). Liner layers were used prior to Al deposition to enhance the quality of the bond pad area. A stack consisting of both tensile and compressed chemical vapor deposition (CVD) oxide layers was deposited and followed by an oxide CMP step to polish the surface. A limited roughness of the top surface after CMP was crucial to yield a high wafer bonding recovery later on. For the heater performance, a partial oxide etch to have a thinner oxide layer on top of the heater area was performed. Afterwards, another sequence of photolithography and dry etch steps were performed to partially form the fluidic inlets and outlets (f). The Heater wafers were then ready for bonding to the combined stack of quartz/fluidic wafers.

Quartz wafer: An opaqued 725 µm thick quartz wafer was used at the top of the wafer stack. On this wafer a thin, high quality SiO layer was deposited follow by polishing using a short CMP to prepare a bondable surface to the fluidic wafer.

Fluidic wafer: A standard Si wafer with a thin-grown SiO layer was fusion bonded with the quartz wafer described above. The silicon wafer was thinned down to 30 µm by a combination of grinding and wet etching process steps. Again, a SiO layer was deposited, followed by CMP to reduce the surface roughness. The fluidic channels were fabricated by photolithography and etch sequences. After cleaning steps, the wafer was ready to bond with the heater wafer.

The fluidic wafer and heater wafer were permanently bonded together with fusion bonding, compression bonding, and curing steps (g). Afterwards, the bottom heater wafer was ground to a thickness of 200 µm to improve the thermal performance of the

heaters. With all three wafers bonded, the fluidic inlet/outlet and bond pad opening areas were created in a single process using photolithography followed by dry etching. Finally, the quartz side of the wafers was de-opaqued resulting in a transparent quartz glass with low autofluorescence properties for optical testing. An image of a fully assembled wafer of sorter chips after dicing is shown in Supplementary Figure S4.

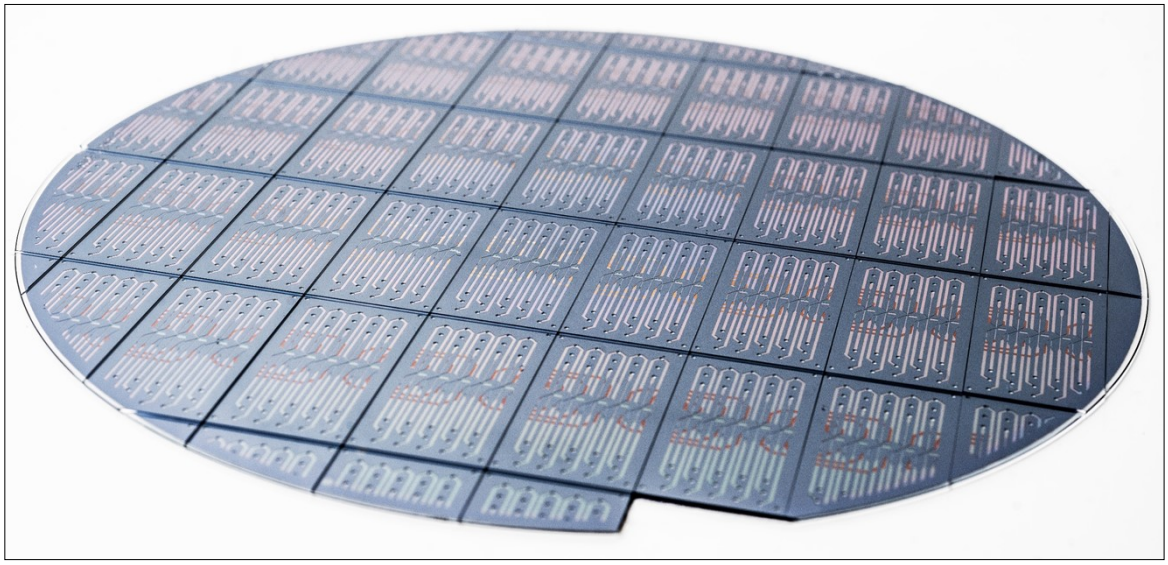

Supplementary Figure S4: Full 200-mm wafer of diced bubble-jet sorting chips as used in this study.

1.3 Recovery calculation

To calculate the recovery, we first require:

- The input purity (r_{in+}) of the sample, which was measured with the FPGA control and data acquisition system (the values were confirmed by cytometer measurements of the input control sample)
- The percentage of targets in the sorted sample (r_{s+}) and waste collection (r_{w+}) which were measured with the conventional cytometer.

With these percentages we can calculate the recovery. We know that the total number of input particles (cells or beads) is N_{tot}, while all positively labelled particles are $N_{tot+} = N_{tot} * r_{in+}$. If we follow all the positive particles and sum them up before and after sorting, we get

$$N_{tot} \cdot r_{in+} = N_{tot} \cdot x \cdot r_{s+} + N_{tot} \cdot (1-x) \cdot r_{w+}$$

Here, x represents the percentage of particles that go to the sorted channel, with all the rest of the particles going to the waste channel ($1-x$). If we solve this equation for x, we can calculate the recovery as

$$Recovery = \frac{all\ sorted\ positve\ particles}{all\ input\ positve\ particles} = \frac{N_{tot} \cdot x \cdot r_{s+}}{N_{tot} \cdot r_{in+}} = x\frac{r_{s+}}{r_{in+}}$$

with

$$x = \frac{r_{in+} - r_{w+}}{r_{s+} - r_{w+}}$$

2 Supplementary results

2.1 Heat accumulation at increased firing rates

Supplementary Figure S5 shows how permanent bubbles accumulated when continuously firing the heater at rates of 1000-2500 Hz. As stated in the article, these bubbles started to form at firing rates of 1500-2000 Hz and spread through the whole heater chamber when the firing rate was further increased (2500 Hz). Their accumulation is correlated with the build-up of heat in the fluid chamber at elevated rates.

In this example test, no flow was applied to the main channel, and the bulk cooling was set to 10°C. Having a flow through the main channel on chip, and thus an increased operation pressure, helped to suppress permanent bubble formation, but the effect was limited. It also must be noted that higher firing rates could be sustained for a short time, but this was not investigated in detail as the focus of this work was on continuous operation.

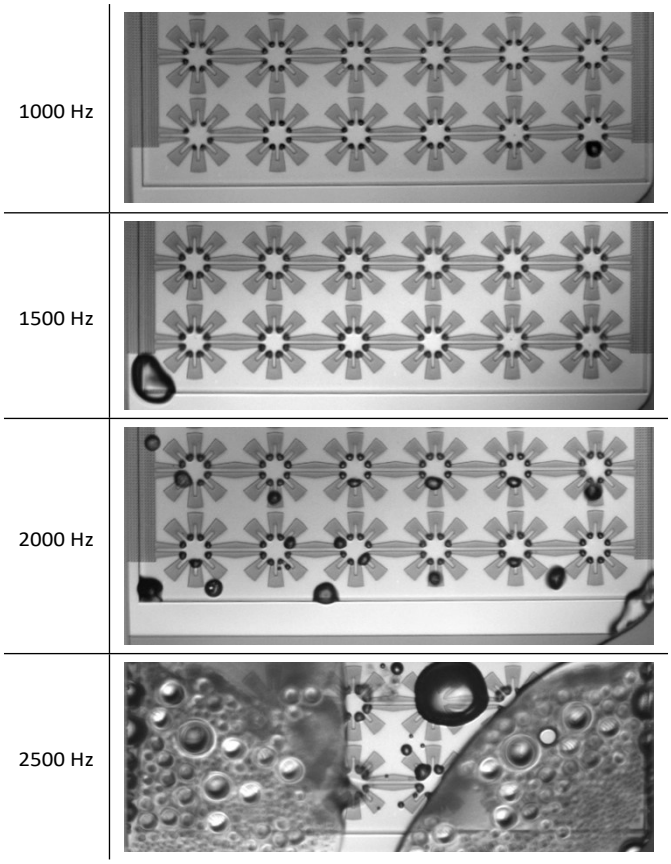

Supplementary Figure S5: Increased firing rates are leading to a temperature increase and the accumulation of permanent bubbles when investigating longer firing periods and continuous operation.

2.2 Performance assessment of an example bead sorting run

This supplementary section provides additional information about the bead sorting run B7 as an example case. The shown data and methods are representative of all other conducted sorting runs. Included is a sequence of a raw data signal which was recorded before the sorting run, an overview of rates and recovery during the run, and post-processing data from the CytoFLEX analysis.

A sample of a raw data signal of run B7 is shown in Supplementary Figure S6. All passing beads are detected by their scatter signal (Det FSC, Det SSC) and positive targets are distinguished by their peak in the fluorescent signal (Det FL). Non-target beads (peaks 6 and 7) do not trigger a sorting, but if a target bead is detected, like in the first five peaks, an electrical pulse is applied (Sorter current). In addition, the fluorescent signal in the verification spot indicates if the sorting was successful. In this snippet, all target beads are sorted correctly, as the number of peaks in the verification spot matches the number of peaks at the detection spot. The data also show that a higher sorting rate can be sustained for a short period. The first five peaks and firings fall into a time window of approximately 1 ms, which would give a sorting rate of 5000 Hz. This is possible because the heater has time after that sequence to cool down again.

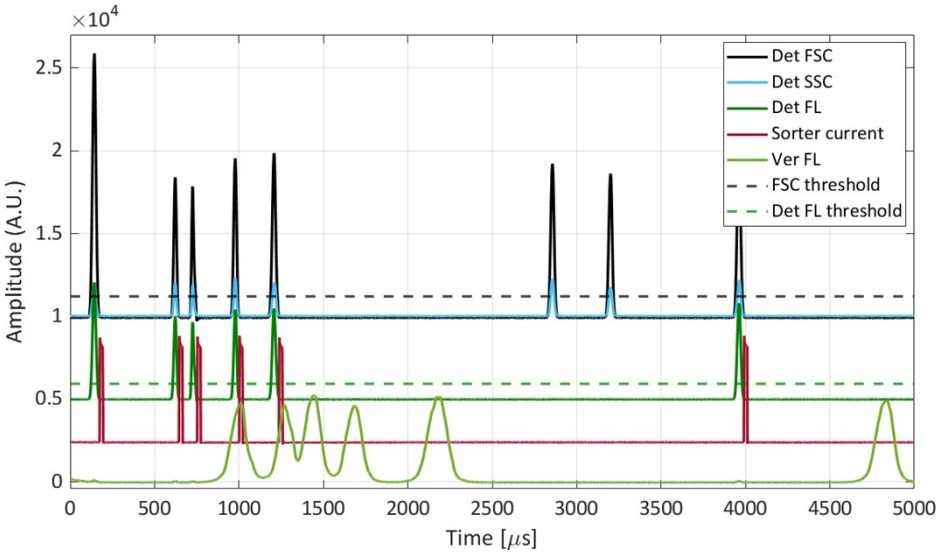

Supplementary Figure S6: Example of logged raw data signal before sorting run B7. Shown are the signals from the detection spot (Det) for forward scatter (FSC), side scatter (SSC), and fluorescence (FL) complemented by the fluorescence signal in the verification spot (Ver FL) and the sorter current. In addition, the threshold levels used for gating are displayed as dashed lines. Signal intensities are displayed in arbitrary units.

Supplementary Figure S7 shows the recorded sorting characteristics based on real-time event data over the runtime of 68 minutes for run B7. The top part shows the total event and target detection rate at the detection spot as well as the rate of verified sorted target beads in the verification spot. Overall, the rates remain relatively constant over the runtime, but some fluctuation remains. As mentioned in the article, the operator can adjust the sample pressure during the run to increase or decrease the event rates. This was done, for example, after some minutes of sorting to get back to a target rate around 1000 Hz after an initial drop in the event rates was observed. The drop in verified targets after 2200 s was caused by the laser shortly switching off for 30 s at the verification spot. However, the sorting performance was not affected as it depends only on the signal from the detection spot. The lower part of the figure shows the evolution of the input purity, which remains constant over the runtime, and the recovery measured at the verification spot. While the feedback on the recovery gives a good indication of sorting efficiency, it is not fully accurate. The main reason is that the fluorescence peaks in the verification spot are not as clearly separated (see Supplementary Figure S6), which increases the chance of inaccurate counting. Therefore, final recovery values for the overview in *Table 1* are based on post-analysis of collected sorted and waste vials with the CytoFLEX cytometer.

An example analysis of the cytometer data is shown in Supplementary Figure S8, again for sorting run B7. First, the gating is set using the data of a control sample of the input vial. Doublet discrimination is performed to gate single beads (top left) and from that gate, the percentage of positive events is extracted (top right). This value is used to confirm the reliability of the input purity value that is measured by the FPGA controller during the run. In this case, the determined value of 61.7% from the separated control sample on the flow cytometer is close to the 62.8% that was measured by the FPGA controller during the run. The two steps of the gating are equally applied when analysing the sorted and waste samples and the results are shown on the bottom left and right, respectively. We can directly read the purity of the sorted fraction as 97.4% and can calculate the recovery, after *eqn.1*, as:

$$Rec = \frac{0.628 - 0.128}{0.974 - 0.128} \cdot \frac{0.974}{0.628} = 91.7\%$$

Following the same approach, the obtained numbers, along with the overall number of detected events and the respective rates, are summarized in *Table 1* for all bead sorting runs. Supplementary Figure S8 shows also how clearly bead samples are separated (into two populations) by signal intensity (envy green). There are two well-separated populations without any overlap.

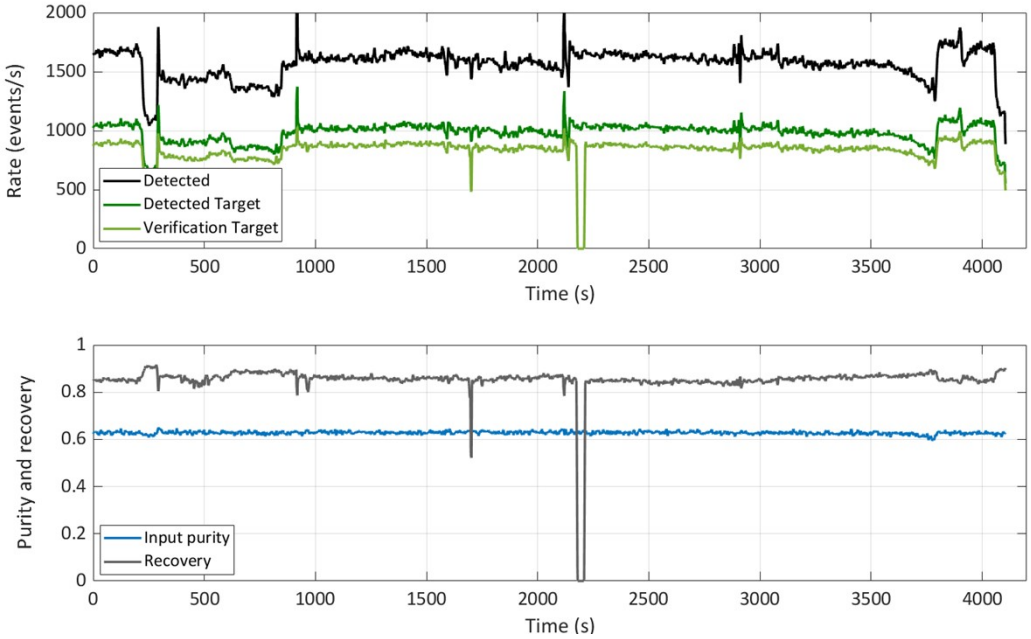

Supplementary Figure S7: Sorting characteristics over the runtime for sorting run B7 with event rates, input purity, and recovery at each second extracted from real-time event data. During the run, the laser in the verification spot switched off for approximately 30 s and no data was recorded (see drop in verification target (top) and recovery (bottom)). However, the sorting performance was not affected as it depends only on the signal from the detection spot. Final purity and recovery values in this work are based on the analysis of the sorted and waste samples on a flow cytometer, not on the shown real-time feedback data.

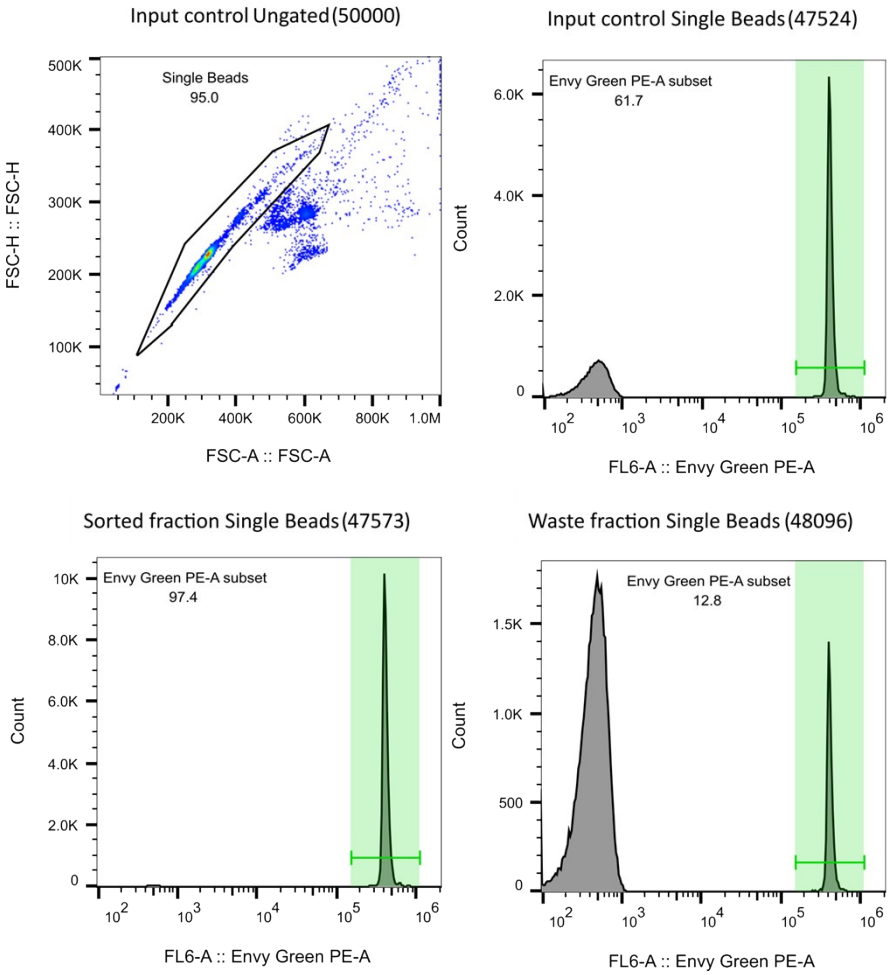

Supplementary Figure S8: Gating and positive fractions in input control (top row), sorted (bottom left), and waste (bottom right) fractions for sorting run B7. The same two-step gating as shown in the top row is also applied for the analysed samples of the sorted and waste fractions.

2.3 Comparison of bead sorting results to previous work

To evaluate the sorting performance, Supplementary Table 1 compares bead sortings results of this work with similar bead sorting results of our previous work.[3] The values from this work are the averages of bead sorting runs B1-B7, while the comparison values are the average of ~1:1 ratio bead sorting tests (test 1-5) in the reference. While the reference work focused also on other sorting tests, such as high rate sorting tests or sorting of rare cells, the chosen data set includes the most similar, and thus most comparable, sorting tests to this works.

Supplementary Table 1: Comparison of sorting experiments in this work and results obtained with the previous sorter chip as described by de Wijs et al.[3] The data are based on the most similar experiment conditions between the two studies, namely sorting runs with mixed bead samples. Values are averaged over the full set of experiments (runs B1-B7 in this work and tests 1-5 in the reference[3]).

	This work	Reference[3]
N° total events	$4.05 \cdot 10^6$	$0.43 \cdot 10^6$
N° target events	$2.61 \cdot 10^6$	$0.18 \cdot 10^6$
Targets/s	1067	614
Purity	98.0%	90.8%
Recovery	88.6%	84.5%

2.4 Performance assessment of an example cell sorting run

The following data are taken from sorting run C1 of *Table 2* in which CD3 positive T cells are isolated from PBMCs. First, Supplementary Figure S9 shows an example sequence of raw data signals that was recorded and processed by the FPGA controller. In contrast to the signal with beads, cells give a wider spectrum of signal intensities, both in the scatter signals (Det FSC, Det SSC) and the fluorescence intensity (FL). This makes gating between the populations based on a simple threshold more difficult. Another observation is the increased number of doublets or clusters. It appears to be more prominent with cells compared to beads (Supplementary Figure S6). Sorting or not sorting a mixed positive-negative cluster always has an impact on either purity or recovery, which could partly explain the slightly lower observed sorting efficiency when sorting cells.

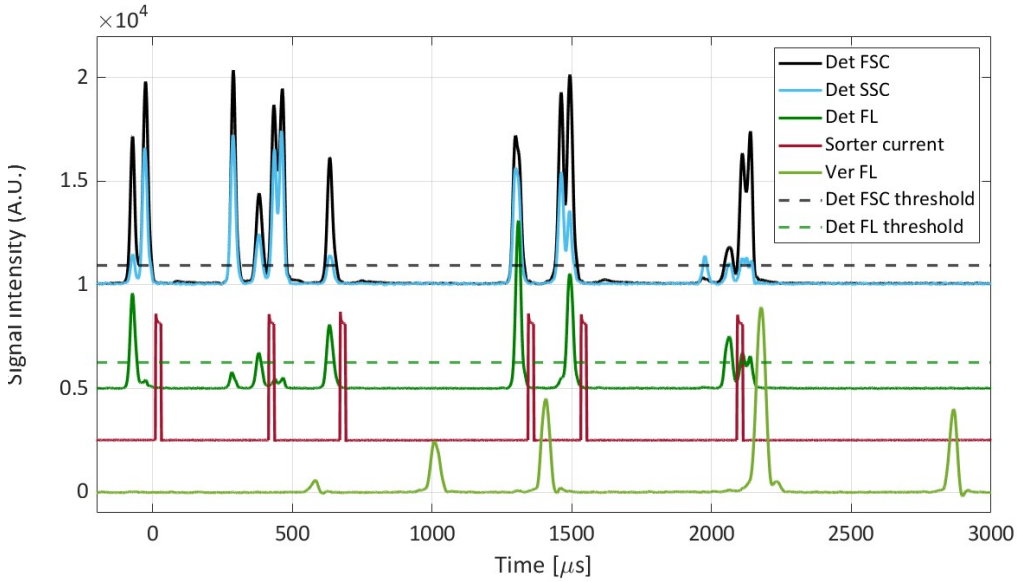

Supplementary Figure S9: Example of logged raw data signal for cell sorting run C1. Shown are the signals from the detection spot (Det) for forward scatter (FSC), side scatter (SSC), and fluorescence (FL) complemented by the fluorescence signal in the verification spot (Ver FL) and the sorting current. In addition, the threshold levels used for gating are displayed as dashed lines. Signal intensities are displayed in arbitrary units. Noticeable is the larger variance in signal intensities compared to beads and the tendency of cells to form doublets or agglomerates.

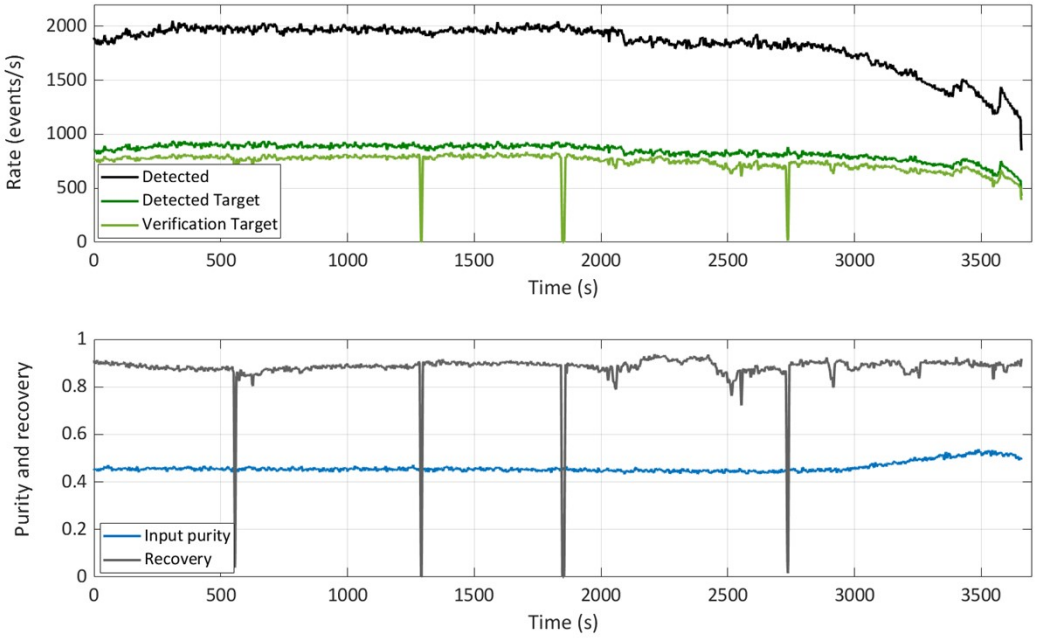

Supplementary Figure S10: Sorting characteristics over the runtime for sorting run C1 with event rates, input purity, and recovery at each second extracted from real-time event data. Final purity and recovery values in this work are based on the analysis of the sorted and waste samples on a flow cytometer, not on the shown real-time feedback data.

Supplementary Figure S10 shows the recorded sorting characteristics based on real time events over the full length of 61 minutes for sorting run C1. Again, the top part shows the detected total and target events at the detection spot as well as the rate of sorted target cells detected at the verification spot. While initially the rates remain very stable, they drop towards the end of the run due to settling in the input sample. The lower part of the figure highlights the input purity as well as the recovery over time extracted from the real-time event data. The input purity remains very stable initially, but changes towards the end of the run. This likely corresponds to the settling of cells in the input vial, where we expect a slight difference in settling speed due to minor differences in density of the different cell populations. On average, the recovery stays at a high level, but sometimes some short-lived drops appear. They can be caused by cell clusters or cells that get stuck at the sorting junction for a short time and affect the signals.

The cytometer results for sorting run C1 are shown in Supplementary Figure S11. As before, the gating in the CytoFLEX system is set using the data of a control sample of the input vial (top row). The target fraction of the input control is 44.8% (bottom left), which is very close to the input purity value r_{in+} of 45.8% that is measured by the FPGA controller for this run. The results for the sorted and waste samples are shown on the bottom centre and right, respectively. This provides us with the purity of the run as 93.0% and allows us to calculate the recovery, after *eqn. 1*, as:

$$Rec = \frac{0.458 - 0.113}{0.93 - 0.113} \cdot \frac{0.93}{0.458} = 85.7\%$$

Following the same approach, the sorting efficiency, along with the overall number of detected events and the respective rates, are summarized in *Table 2* for all cell sorting runs.

In Supplementary Figure S11 it is clearly visible that different populations of cells from the PBMC sample overlap in fluorescence intensity (see input control in bottom left). The target population with positive CD3-PE signal intensity is adjacent to the negative fraction and is not as clearly separated as for beads. This is expected but can influence the sorting efficiency as discussed in the *Sorting* section.

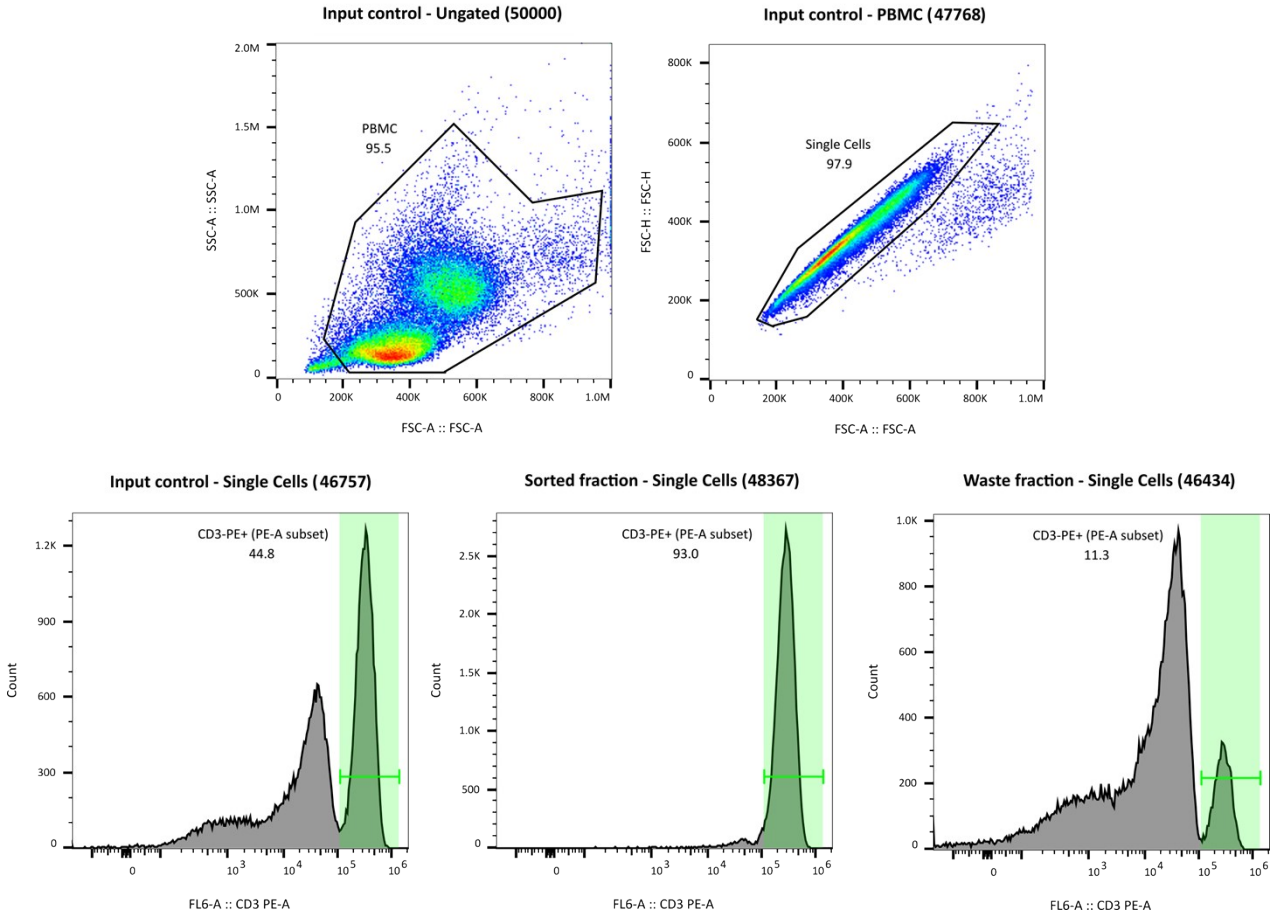

Supplementary Figure S11: Gating strategy for PBMCs and single cells (top row) and CD3-PE positive fractions in the input control, waste, and sorted sample (bottom row) for sorting run C1.